

Molecular Dynamics of Excited State Intramolecular Proton Transfer: 2-(2'-Hydroxyphenyl)-4-methyloxazole in Gas Phase, Solution, and Protein Environments[†]

Oriol Vendrell,[‡] Miquel Moreno,[‡] José M. Lluch,[‡] and Sharon Hammes-Schiffer^{*,§}

Departament de Química, Universitat Autònoma de Barcelona, 08193, Bellaterra (Barcelona), Spain, and Department of Chemistry, 152 Davey Laboratory, Pennsylvania State University, University Park, Pennsylvania 16802

Received: December 2, 2003; In Final Form: January 21, 2004

The ultrafast enol–keto photoisomerization in the lowest singlet excited state of 2-(2'-hydroxyphenyl)-4-methyloxazole (HPMO) is investigated using classical molecular dynamics in conjunction with an empirical valence bond potential. This process is studied in four different environments: the gas phase, dimethyl sulfoxide, water, and human serum albumin protein. The effects of the environment on the proton transfer time and the promoting-mode motions are analyzed. The ring–ring in-plane bending of HPMO is identified as the dominant low-frequency vibrational mode that decreases the proton donor–acceptor distance to facilitate proton transfer. The mean proton transfer times are 100–200 fs in all of the environments. The population decay of the enol tautomer in the S_1 state is significantly slower for the reaction in water than in DMSO and protein. The slower population decay in water is found to arise from configurations with intermolecular hydrogen bonds between HPMO and water molecules, leading to a disruption of the intramolecular hydrogen bond in HPMO. All of the condensed-phase environments are found to dampen the donor–acceptor vibrational mode after the proton transfer process, thereby stabilizing the keto tautomer. In the gas phase, the donor–acceptor mode oscillations continue to facilitate the forward and reverse isomerization processes.

1. Introduction

Excited state intramolecular proton transfer (ESIPT) reactions play an important role in many biological processes^{1–4} as well as in a variety of technological applications such as photostabilizers,⁵ UV filter materials,⁶ and electronic devices.⁷ As a result, these types of reactions have been extensively investigated both experimentally^{1,8–18} and theoretically.^{14,19–27} The observation of a large Stokes shift in the emission spectra has provided evidence of the proton transfer tautomer after photoexcitation. Ultrafast techniques have been used to track the populations of different species on femtosecond time scales. These experimental techniques have provided substantial insight and understanding into the underlying dynamics of ESIPT reactions.

ESIPT reactions involving enol–keto isomerization after photoexcitation from the singlet ground electronic state (S_0) to the lowest singlet excited state (S_1) are particularly relevant to biological processes. In these reactions, the proton transfer is due to fundamental changes in the potential energy surface upon excitation. A variety of enol–keto isomerization systems have been investigated both experimentally and theoretically. For most of these systems, the ultrafast dynamics experiments indicate a barrierless or near-barrierless process^{10–12,15,16} in which the proton is transferred in less than 300 fs. Calculations at various levels of theory for small model systems also indicate a barrierless or near-barrierless mechanism.^{21–26} The participa-

tion of low-frequency vibrational modes that make the proton transfer possible by lowering or eliminating the proton transfer barrier has also been established.^{10,11} These low-frequency modes involve heavy-atom motion and are often referred to as promoting modes.

This paper focuses on the photoisomerization of 2-(2'-hydroxyphenyl)-4-methyloxazole (HPMO), as depicted in Figure 1. The femtosecond dynamics of this process have been studied in 3-methylpentane¹⁵ and *para*-dioxane¹ solvents, nanocavities such as cyclodextrins, and a protein environment.^{1,15,16} The experimental studies of ESIPT from the enol to keto HPMO forms monitored in aprotic solvents and supramolecular environments^{1,15,16} indicate that the proton transfer time ranges from 100 to 200 fs with virtually no dependence on the environment.

These types of ESIPT processes have been studied theoretically using several approaches. Electronic structure methods have been used to identify stationary points on the S_1 potential energy surface. For example, the HPMO molecule encapsulated in β -cyclodextrin was studied by some of us using hybrid quantum mechanical/molecular mechanical (QM/MM) methods.¹⁹ Semiclassical dynamics calculations²⁰ in which all vibrational modes except the proton and donor–acceptor coordinates were treated as harmonic oscillators have been conducted on a full-dimensional gas-phase model of 2-(2'-hydroxyphenyl)-oxazole. In addition, fully quantum dynamical calculations of ESIPT keto–enol isomerization processes have been performed recently for a reduced 7D potential energy surface.²⁸ These semiclassical and fully quantum dynamical approaches provide a rigorous treatment of the nuclei at the cost of using a potential energy surface with reduced dimensions or harmonic oscillators for the majority of modes. Another limitation of these methods is that the wave packet can be

[†] Part of the special issue “Hans C. Andersen Festschrift”.

^{*} Author to whom correspondence should be addressed. E-mail: shs@chem.psu.edu.

[‡] Universitat Autònoma de Barcelona.

[§] Pennsylvania State University.

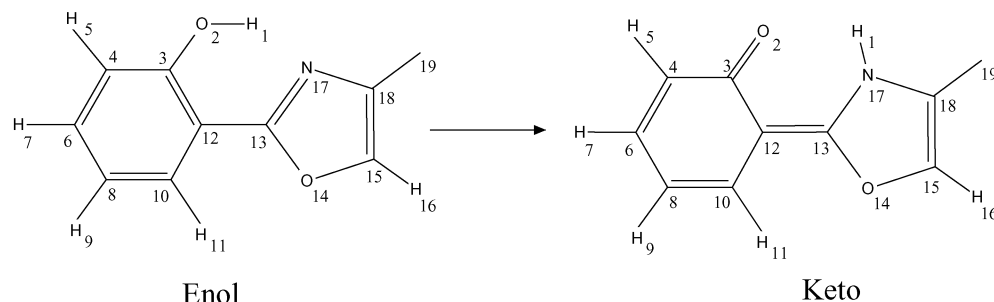


Figure 1. Schematic illustration of proton transfer in HPMP.

propagated for only relatively short times. Unfortunately, the explicit inclusion of a complex environment in semiclassical and fully quantum dynamical calculations is currently not computationally practical. As a result, alternative approaches have been developed to include the significant nuclear quantum effects for proton transfer reactions in condensed phases.^{29–34}

In this paper, we present a classical molecular dynamics study of the ESIPT reaction for HPMP in the gas phase, in the aprotic solvent dimethyl sulfoxide (DMSO), in the protic solvent water, and at the binding site I of the protein human serum albumin (HSA). The main objective of this study is to elucidate the effect of the environment on the ESIPT process. The classical dynamical treatment of the nuclei is justified by the ultrafast nature of the process and the barrierless mechanism. Moreover, femtosecond studies in related systems have shown no isotope effect for the ESIPT process when the proton is substituted with deuterium.⁹ Our implementation of classical molecular dynamics in conjunction with an empirical valence bond (EVB)^{35–41} potential enables us to propagate hundreds of trajectories in real time for the excited state proton transfer process in each environment. These calculations provide detailed microscopic information about the ESIPT process in various environments as well as statistically averaged properties for comparison to macroscopic observables such as the experimentally measured rates. The paper is organized as follows. Section 2 describes the theoretical models, the EVB potential, and the simulation procedure. Section 3 presents the results and analysis for the four different environments. Section 4 summarizes the results and the overall conclusions.

2. Methods

2.1. Model Systems. The model systems used in the condensed-phase simulations are depicted in Figure 2. For the simulations in DMSO, the HPMP molecule was placed in a cubic box of side 30 Å with 344 solvent molecules, resulting in a total of 1395 atoms. The simulations in H₂O were performed in a cubic box of side 30 Å with 1329 solvent molecules, resulting in a total of 4006 atoms. For the simulations in the protein HSA, the initial coordinates were obtained from the 1HA2 entry⁴² in the Protein Data Bank. The 1HA2 structure has a bound warfarin molecule, which is an aromatic molecule of similar size to HPMP. Warfarin was substituted by HPMP prior to equilibration. The protonation states for residues with polar side chains were determined at pH 7. The protonation states for the His residues were determined by an examination of the hydrogen-bonding structures. The protein was immersed in a box of dimensions 63 × 89 × 98 Å³ with 15 565 water molecules, resulting in a total of 52 537 atoms.

GROMOS force field^{43,44} 43A1 was used to describe the solvent and protein environments. The *S*₀ electronic ground state potential for the HPMP enol tautomer was constructed using

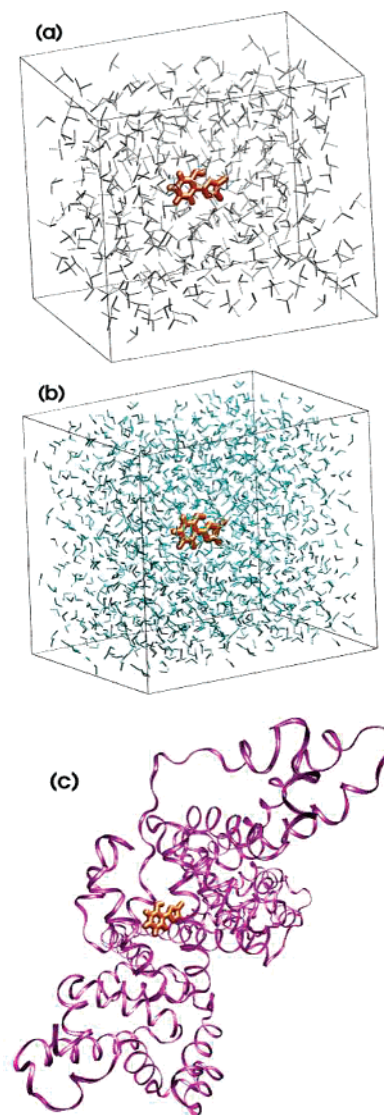


Figure 2. Snapshots of the unit cells for the models of HPMP in (a) DMSO, (b) H₂O, and (c) human serum albumin simulations. In c, the solvent is omitted for clarity. HPMP is orange in a–c.

atom types and geometrical parameters of the 43A1 force field. The charges for the HPMP molecule were assigned on the basis of similar functional groups belonging to the 43A1 force field. The potential for the first singlet excited electronic state (*S*₁) was represented by the two-state EVB model described below.

2.2. *S*₁ EVB Potential. The *S*₁ potential energy surface was represented by a two-state EVB model.^{35,37,41} EVB state 1 corresponds to the enol form of HPMP, where the H1 proton is bonded to the O2 oxygen, and EVB state 2 corresponds to the keto form, where the proton is bonded to the N17 nitrogen atom. (See Figure 1.) The *S*₁ electronic adiabatic state is the

lowest energy eigenvalue of the EVB matrix in eq 1:

$$H_{\text{el}}(\mathbf{Q}) = \begin{pmatrix} V_{11}(\mathbf{Q}) & V_{12}(\mathbf{Q}) \\ V_{12}(\mathbf{Q}) & V_{22}(\mathbf{Q}) + \Delta \end{pmatrix} \quad (1)$$

\mathbf{Q} represents the set of all nuclear coordinates of the HPMO molecule and the environment. The coupling term was chosen to be constant so that $V_{12}(\mathbf{Q}) \equiv V_{12}$. This EVB potential was parametrized by fitting to gas-phase electronic structure calculations. All electronic structure calculations were performed with the Gaussian 98 program⁴⁵ using the 6-31G(d,p) basis set, and the time-dependent density functional theory (TDDFT)⁴⁶ calculations used the B3LYP⁴⁷ functional. We emphasize that only a qualitatively reasonable potential energy surface is required to address the objectives of this study.

The $V_{11}(\mathbf{Q})$ and $V_{22}(\mathbf{Q})$ matrix elements were based on the GROMOS 43A1 force field with the parameters for the corresponding protonation states. The bonding parameters in the ring system correspond to the enol ground state for both EVB states, but the effects of electronic rearrangement in the excited state were included implicitly by fitting the EVB parameters to TDDFT excited-state calculations that include these electronic rearrangements. The enol and keto equilibrium structures were determined by geometry optimization at the configuration interaction singles (CIS)⁴⁸ level. The charges on each atom in the electronically excited HPMO molecule were assigned by modifying the GROMOS charges on the ground-state HPMO molecule on the basis of the differences between S_1 and S_0 charges obtained with the natural population analysis⁴⁹ at the CIS and Hartree–Fock levels, respectively. This strategy is based on the differences in charges for the S_1 and S_0 states rather than the calculated values for the S_1 state in order to maintain consistency between the partial charges and the Lennard-Jones parameters within the GROMOS force field. The partial charges were chosen to be the same for the two EVB states because the partial charges calculated at the CIS level with the natural population analysis were virtually identical for the excited-state enol and keto tautomers. The C12–C13 bond, C3–C12–C13 and C12–C13–N17 angles, and H1–O2–C3–C12 and H1–N17–C13–C12 dihedrals were reparametrized to account for the S_1 -state ring–ring bending mode as well as the out-of-plane hydrogen atom movement. This reparametrization procedure involved fitting to the TDDFT singlet excited state calculations for geometries in which each bond or angle was systematically perturbed from the CIS equilibrium structure. The modified GROMOS parameters are given in Supporting Information. In addition, the 43A1 force field was modified to describe the donor–proton bond in V_{11} and the acceptor–proton bond in V_{22} by a Morse function:

$$V_{\text{Morse}}(r_i) = D_i(1 - e^{-\beta_i(r_i - r_i^0)})^2 \quad (2)$$

r_1 is the donor–proton distance, and r_2 is the acceptor–proton distance.

The Morse potential parameters as well as the V_{12} and Δ parameters were fit to a linear reaction path proton transfer potential energy profile for the singlet excited state. First, the geometries along the linear reaction path were generated between the equilibrium enol and keto structures determined by geometry optimization at the CIS level. Subsequently, the linear reaction path proton transfer potential energy profile was obtained by calculating the singlet excited state energies of the enol, keto, and all interpolated structures with TDDFT. The lowest-energy eigenvalue of the EVB matrix in eq 1 was fit to

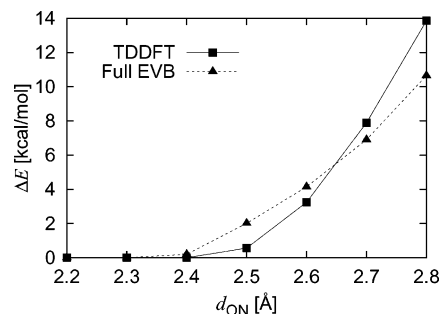


Figure 3. Proton transfer barrier as a function of the donor–acceptor distance calculated with the TDDFT method and the full EVB potential. The structures along the proton transfer potential energy profiles were determined from constrained geometry optimizations at the CIS level.

TABLE 1: Parameters for the Two-State EVB Model

D_1	62.14 kcal/mol
D_2	65.73 kcal/mol
β_1	2.1 Å ^{−1}
β_2	2.0 Å ^{−1}
r_1^0	0.95 Å
r_2^0	1.0 Å
V_{12}	32.26 kcal/mol
Δ	−6.69 kcal/mol

reproduce the linear reaction path proton transfer potential energy profile. To simplify this fitting procedure, a reduced EVB potential that includes only the Morse potential terms of HPMO and Δ for the diagonal elements was used for this parametrization. There are eight parameters in this reduced EVB potential—six corresponding to the $V_{\text{Morse}}(r_1)$ and $V_{\text{Morse}}(r_2)$ terms (r_i^0 , D_i , and β_i for each Morse potential) and the V_{12} and Δ parameters. These eight parameters were fit to the energies of the linear reaction path structures with a nonlinear least-squares fitting procedure. The initial values of the Morse parameters were chosen to be consistent with the ground-state bond lengths, dissociation energies, and frequencies, and the initial value for Δ was chosen to be the energy difference between the enol and keto forms calculated at the CIS level.

To refine the EVB potential further, we investigated the dependence of the proton transfer barrier on the donor–acceptor distance. For each donor–acceptor distance d_{ON} , the structures along the proton transfer potential energy profile were obtained through a series of geometry optimizations at the CIS level with constrained donor–acceptor and donor–proton distances. The relative energies of the structures at the top of the barrier and at the reactant minimum were calculated with TDDFT for the proton transfer potential energy profile corresponding to each donor–acceptor distance. The resulting proton transfer barrier heights are depicted in Figure 3. After the nonlinear least-squares fitting procedure to the linear reaction path, the V_{12} and Δ parameters were varied to fit the dependence of the proton transfer barrier on the donor–acceptor distance for the structures generated at the CIS level. A comparison of the full EVB and TDDFT proton transfer barriers is depicted in Figure 3. Note that the proton transfer barrier vanishes at approximately the same donor–acceptor distance for the full EVB and TDDFT calculations. Moreover, the qualitative agreement at larger donor–acceptor distances is adequate for the purposes of this paper. The final values of the parameters determined by the fitting procedure are given in Table 1.

As an additional test of the EVB potential, we generated the potential energy surfaces as functions of the donor–proton and donor–acceptor distances. The structures for these potential energy surfaces were obtained with constrained geometry

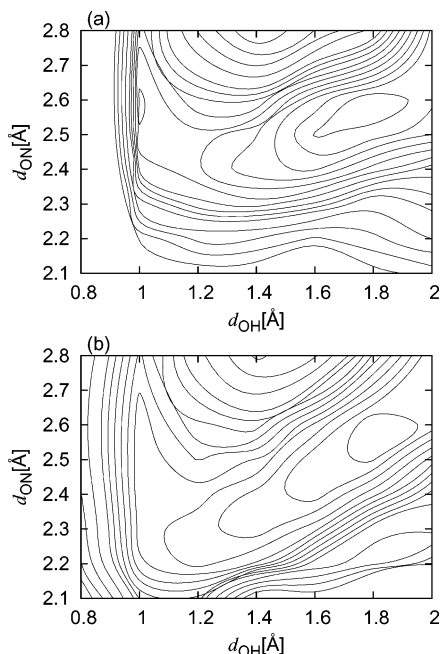


Figure 4. Potential energy surfaces as functions of the donor–acceptor (d_{ON}) and donor–proton (d_{OH}) coordinates calculated with (a) the TDDFT method and (b) the full EVB potential. The structures were obtained from constrained geometry optimizations at the CIS level.

optimizations at the CIS level. The energies of these structures were calculated with both the TDDFT method and the full EVB potential. The resulting 2D potential energy surfaces are depicted in Figure 4. The qualitative agreement between these potential energy surfaces indicates that the EVB potential is adequate for the studies described below.

2.3. Simulation Procedure. The simulations were performed within the framework of the GROMOS⁴³ program. For all simulations in condensed phases, the cutoff radius for nonbonded interactions was set to 14 Å, and the nonbonded interactions between 8 and 14 Å were calculated only every five molecular dynamics steps. Outside the sphere of radius 14 Å, the electrostatics were represented by a reaction field with a relative dielectric constant of 62.3 for SPC/E water⁵⁰ and 30.0 for DMSO,⁵¹ as determined for the solvent models used in the simulations. The SHAKE⁵² algorithm was used to constrain the internal solvent bonds as well as all bonds involving hydrogen atoms except the transferring hydrogen atom.

Each model system described above was equilibrated with the S_0 parametrization of the HPMO molecule. The integration time step for the equilibration was 2 fs. Two separate Berendsen thermostats⁵³ with relaxation times of 0.1 ps each were used to maintain the temperature of both solute and solvent molecules at 300 K. For the gas-phase and solvent models, the equilibration procedure involved two steps, each consisting of steepest descent minimization followed by 8 ps of molecular dynamics. Subsequently, 200 ps of molecular dynamics was performed to ensure thermal equilibrium. The protein model was equilibrated in four steps, gradually releasing the force constant of position restraints to the crystal structure positions from 100 to 50, 25, and 0 kcal/(mol Å²). Each step consisted of a steepest descent minimization followed by 5 ps of molecular dynamics. Subsequently, 200 ps of molecular dynamics without any restraints on the crystal structure positions was performed to ensure equilibration.

Initial configurations for the classical molecular dynamics trajectories in the S_1 state were selected from a thermal equilibrium distribution at 300 K of the S_0 state. For each environment studied, 400 ps of molecular dynamics was

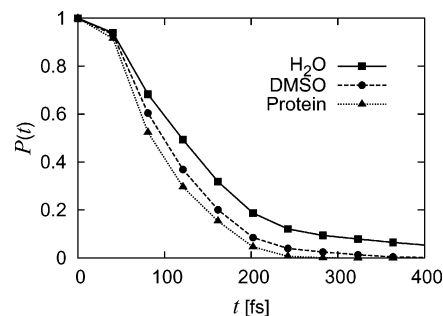


Figure 5. Population decay of the enol tautomer as a function of time for the proton transfer reaction in water, DMSO, and HSA protein.

TABLE 2: Mean Proton Transfer Time (T_{PT}) for Each Simulated Environment

	$T_{\text{PT}}(\text{fs})$
gas phase	132
DMSO	112
H ₂ O	134
HSA	101

performed in the S_0 state, and a configuration was saved every 2 ps to obtain 200 initial configurations. The initial velocities were sampled from a Boltzmann distribution using a different random seed for each configuration to avoid time correlation between the selected initial configurations.

Each initial configuration and set of velocities was evolved using classical molecular dynamics on the two-state EVB potential energy surface representing the S_1 electronic state. The excited electronic state molecular dynamics simulations were performed without thermal bath coupling. A time step of 0.5 fs was used, and each trajectory was integrated for a total time of 4 ps.

3. Results and Discussion

We calculated the mean proton transfer time (T_{PT}) for each set of trajectories in the gas phase, DMSO, H₂O, and protein. To our knowledge, no experimental results in water have been reported, although results in other polar protic environments have been described. The proton transfer time is defined as the time for the distance between the proton and acceptor atoms to become smaller than 1.1 Å following photoexcitation. The results in Table 2 illustrate that the mean proton transfer times are similar for the reaction in the gas phase, DMSO, water, and HSA. These calculated values are consistent with experimental measurements of proton transfer times ranging from 100 to 200 fs for various aprotic solvents and supramolecular environments.^{1,15,16}

We also investigated the population decay of the enol tautomer in the S_1 state. The enol population decay $P(t)$ is defined as

$$P(t) = \frac{\text{nonreacted traj at time } t}{\text{total no. of traj}} \quad (3)$$

Figure 5 depicts $P(t)$ for the three condensed-phase environments. This figure indicates that the enol population decay is faster for the DMSO and HSA environments than for the water environment. At 200 fs, 18% of the trajectories in water have not yet reacted, but only 6.1% and 1.0% of the trajectories in DMSO and HSA, respectively, have not reacted. Similarly, at 400 fs, 5.4% of the trajectories in water have not yet reacted, but all trajectories in DMSO and HSA have reacted. The slower enol population decay for water in comparison to those for

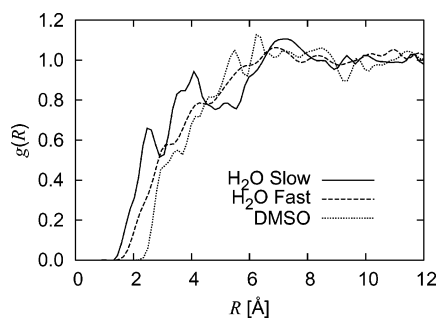


Figure 6. Radial distribution functions of the solvent molecules with respect to the transferring proton averaged over the first 100 fs of dynamics for the reaction in water and DMSO. For the reaction in water, slow trajectories refer to those that react in more than 300 fs, and fast trajectories refer to those that react in less than 100 fs.

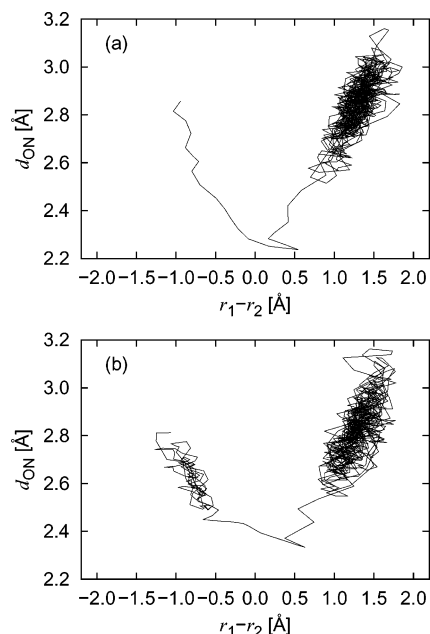


Figure 7. Two trajectories in water projected onto the proton coordinate $r_1 - r_2$ and the donor-acceptor coordinate d_{ON} . The proton transfer times are 70 and 710 fs for the trajectories in a and b, respectively.

DMSO and HSA is consistent with the slightly larger mean proton transfer time for water given in Table 2.

To elucidate the differences between water and the other environments, we evaluated the radial distribution function of the solvent molecules with respect to the transferring proton for both water and DMSO solvents. Two different sets of trajectories were examined for the water case: the “slow” trajectories that react in more than 300 fs and the “fast” trajectories that react in less than 100 fs. The radial distribution function was averaged over the first 100 fs for these two sets of water trajectories and for all of the DMSO trajectories. The results are depicted in Figure 6. Although the average distance between the transferring proton and the solvent molecules is larger for DMSO than for H₂O, the qualitative shape of the radial distribution function is similar for the DMSO trajectories and for the fast trajectories in water. In contrast, for the slow trajectories in water, the proton forms an intermolecular hydrogen bond with a water molecule that must be broken before the proton can transfer. The evidence for this intermolecular hydrogen bond is the peak at ~ 2.3 Å in the radial distribution function for the slow trajectories in water. This peak is not observed for the fast trajectories in water or for the DMSO trajectories. The DMSO molecules do not approach close enough

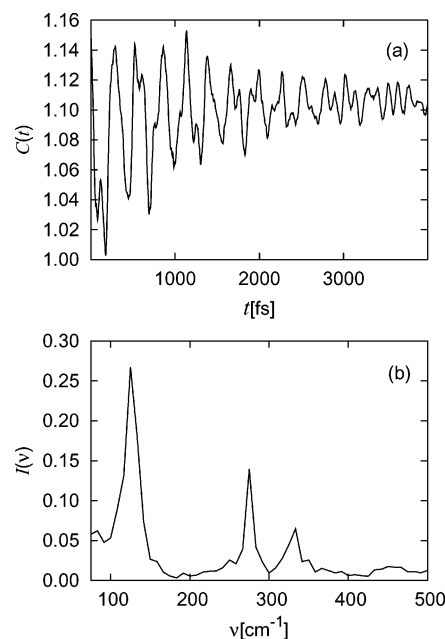


Figure 8. (a) Autocorrelation function of the donor-acceptor coordinate d_{ON} . (b) Modulus of the Fourier transform of the autocorrelation function in a.

to the HPMO molecule to form intermolecular hydrogen bonds in the simulations. This type of solute-solvent hydrogen-bonding effect in water has been observed previously in theoretical studies of other proton transfer systems.⁵⁴

Analyses of individual trajectories in water also indicate that the slow trajectories start from configurations in which the intramolecular hydrogen bond is not formed because of hydrogen-bonding interactions with surrounding water molecules. Figure 7 depicts two representative trajectories from the simulations in water. Figure 7a illustrates a proton transfer trajectory that reacts in 70 fs and thus corresponds to the fast proton transfer regime. At the time of excitation, the intramolecular hydrogen bond is well formed, and no solvent molecules are strongly interacting with the donor oxygen, the acceptor nitrogen, or the transferring hydrogen atom. In this case, the donor-acceptor distance quickly decreases to ~ 2.3 Å, leading to a barrierless reaction pathway. In contrast, Figure 7b illustrates a proton transfer trajectory that reacts in 710 fs. In this case, hydrogen-bonding interactions of the HPMO molecule with the solvent water molecules must be broken before the proton transfers. As a result, the system is trapped in the reactant region until the intramolecular hydrogen bond is formed, thereby enabling the donor-acceptor distance to decrease enough to eliminate the proton-transfer barrier.

Experimental data provide support for the possibility of a slower process due to intermolecular interactions between the solute and the solvent. In femtochemistry experiments on HPMO in jet-cooled conditions, an emission assigned to the enol tautomer appeared when small amounts of methanol were added to the sample.¹³ This emission was not observed without the protic solvent and may be related to the slow proton transfer trajectories found in the water simulations. In more recent experiments for an ESIPT process on a different system, 3-hydroxyflavone,¹⁸ a subpicosecond rising component from the keto tautomer product was observed in all solvents, but an additional slower picosecond rising component from the keto tautomer product was observed in highly polar and protic solvents. The additional rising component in highly polar and protic solvents was assigned to molecules that must break

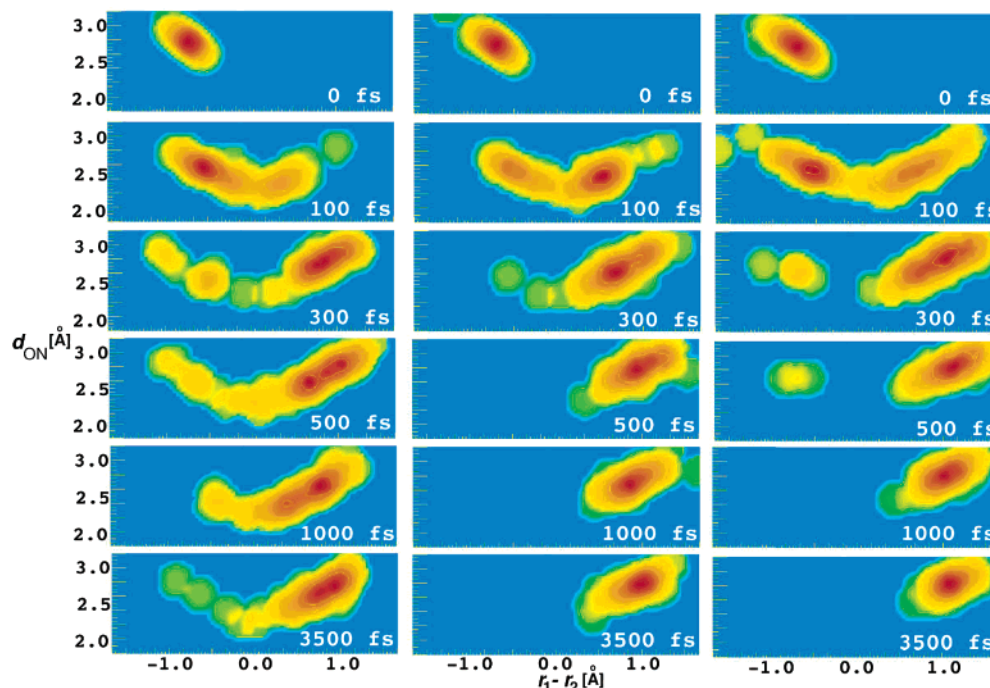


Figure 9. Classical probability density for the proton and donor–acceptor coordinates $r_1 - r_2$ and d_{ON} for trajectories in the gas phase (left), DMSO (middle), and water (right). Red indicates high density, and blue indicates low density.

intermolecular interactions prior to the intramolecular proton transfer.

We also studied the character of the promoting mode, which is defined to be the donor–acceptor vibrational mode for this process. As shown in Figure 3, the donor–acceptor distance significantly influences the proton transfer barrier. The donor–acceptor vibrational frequency was obtained from the autocorrelation function $C(t)$ of the donor–acceptor distance for the excited-state dynamics trajectories in the gas phase. The autocorrelation function is defined as

$$C(t) = \frac{\langle d_{\text{ON}}(t) d_{\text{ON}}(0) \rangle}{\langle d_{\text{ON}}(0) d_{\text{ON}}(0) \rangle} \quad (4)$$

where the brackets $\langle \dots \rangle$ represent an average over the ensemble of excited-state trajectories. The autocorrelation function is given in Figure 8a, and the modulus of its Fourier transform is given in Figure 8b. The dominant component in the promoting-mode vibration is the ring–ring in-plane bending, which corresponds to the peak centered at $\sim 120 \text{ cm}^{-1}$. This observation is consistent with our calculation of the harmonic frequencies at the CIS level for the keto tautomer, where the frequency of the ring–ring in-plane bending mode was found to be 147 cm^{-1} . Other vibrational motions with higher frequencies also contribute to the promoting mode, although they have smaller amplitudes.

To provide additional information about the evolution of the system, we calculated the classical probability density defined as

$$\rho(x', y', t) = \frac{1}{N} \sum_{i=1}^N \delta(x_i(t) - x') \delta(y_i(t) - y') \quad (5)$$

for each environment. Here, N is the number of excited-state trajectories, $x_i(t)$ denotes $r_1 - r_2$ for trajectory i at time t , and $y_i(t)$ denotes d_{ON} for trajectory i at time t . The classical probability densities for the reaction in the gas phase, DMSO, and water are depicted in Figure 9. The HSA classical probability density looks very similar to the DMSO density and

is not included in the figure. For the trajectories in water, a significant amount of density remains in the reactant region after 500 fs because of hydrogen bonding between HPMO and the surrounding water molecules. In contrast, for the trajectories in DMSO and protein, a negligible amount of density remains in the reactant region by 500 fs. For the gas-phase trajectories, a significant amount of density returns to the reactant region after the proton transfer reaction because of continued oscillations of the donor–acceptor mode.

The basic differences between gas-phase and condensed-phase trajectories are illustrated by Figures 10 and 11. A typical gas-phase trajectory is represented in Figure 10. In this gas-phase trajectory, the donor–acceptor oscillations enable the system to return to the reactant region (i.e., the distance between the proton and the donor becomes less than 1.1 Å) several times. The crossings between the reactant and product regions are indicated in Figure 10b when $r_1 - r_2 = 0$. In contrast, for the trajectories in solvent and protein, the system remains in the product region after the proton transfer reaction because the donor–acceptor distance remains in the range of 2.5 to 3 Å . A typical trajectory in DMSO is represented in Figure 11. In these condensed-phase systems, the energy from the promoting mode is quickly transferred to the other modes of the HPMO or to the environment following the proton transfer.

4. Conclusions

In this paper, we studied the ultrafast enol–keto isomerization in the lowest singlet excited state (S_1) of 2-(2'-hydroxyphenyl)-4-methyloxazole (HPMO). This process involves an intramolecular proton transfer from an oxygen atom to a nitrogen atom. We have examined this reaction in four different environments: the gas phase, DMSO, water, and hydrophobic binding site I of the human serum albumin protein. The potential energy surface for the S_1 electronic state was described with a two-state EVB potential parametrized to reproduce TDDFT calculations. The photoexcitation was modeled by equilibration in the ground state, followed by instantaneous promotion to the S_1 state. The excited-state dynamical process was studied with

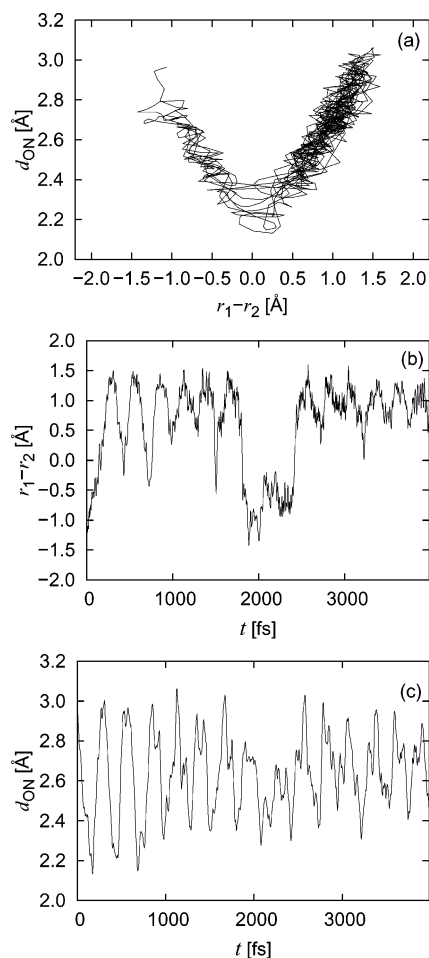


Figure 10. Analysis of a representative gas-phase trajectory: (a) projection onto the proton and donor–acceptor coordinates $r_1 - r_2$ and d_{ON} ; (b) time evolution of $r_1 - r_2$; (c) time evolution of d_{ON} .

classical molecular dynamics for the four different environments. The mean proton transfer times were calculated to be 100–200 fs in all four environments. These calculated values are consistent with experimental data indicating that the proton-transfer time ranges from 100 to 200 fs and is virtually independent of the environment for various aprotic solvents and supramolecular environments.^{1,15,16}

In the gas-phase reaction, the enol–keto isomerization is barrierless. We have identified the ring–ring in-plane bending of HPMO as the dominant low-frequency ($\sim 120 \text{ cm}^{-1}$) vibrational mode that decreases the proton donor–acceptor distance, thereby facilitating the proton transfer reaction. In the gas-phase molecular dynamics simulations, the majority of trajectories reacted in less than 200 fs, and virtually all of the trajectories reacted by 400 fs. After the proton transfers, however, the donor–acceptor mode continues to oscillate in such a way that the proton occasionally transfers back to the donor, leading to the enol tautomer. The forward and reverse isomerization processes continue to occur in the gas phase.

In contrast to the reaction in the gas phase, the condensed-phase systems remain in the product (i.e., the keto tautomer) after the proton transfer process. The return to the enol tautomer is not feasible in condensed phases because the energy from the promoting mode is quickly transferred to the modes of the environment, thereby damping the donor–acceptor oscillation. As a result, the donor–acceptor distance does not become short enough to enable the reverse proton transfer reaction. This effect is expected to be a common feature of most condensed-phase

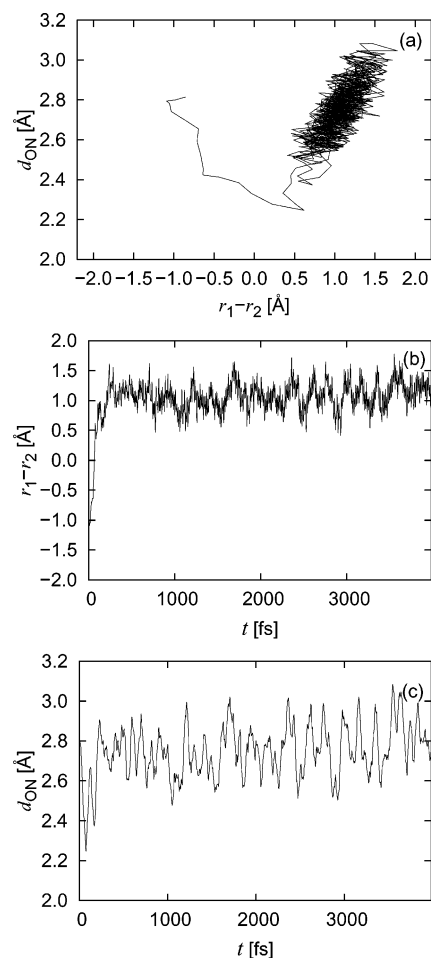


Figure 11. Analysis of a representative trajectory in DMSO: (a) projection onto the proton and donor–acceptor coordinates $r_1 - r_2$ and d_{ON} ; (b) time evolution of $r_1 - r_2$; (c) time evolution of d_{ON} .

environments, except possibly for solvents with very low friction.

The basic features of the isomerization reaction are different in a polar, protic solvent such as water than in DMSO and protein. An analysis of the simulation data indicates that the population decay of the enol tautomer in the S_1 state is significantly slower for the reaction in water than in DMSO and protein. The slower population decay in water arises from configurations with intermolecular hydrogen-bonding interactions between HPMO and water molecules, leading to a disruption of the intramolecular hydrogen bond in HPMO. In the absence of the intramolecular hydrogen bond in HPMO, the donor–acceptor distance does not decrease sufficiently to facilitate the fast proton transfer reaction. This effect is expected to be a general feature in highly polar and protic solvents. Moreover, these results are consistent with experimental studies of these types of processes in polar solvents.^{13,18}

The simulations presented in this paper provide insight into fundamental aspects of excited-state intramolecular proton-transfer reactions. The results and analyses elucidate the effects of different environments on these types of processes. This insight is relevant to a wide range of biologically and technologically important processes.

Acknowledgment. O.V., M.M., and J.M.L. are grateful for financial support from the Spanish Ministerio de Ciencia y Tecnología and the Fondo Europeo de Desarrollo Regional through project no. BQU2002-00301. O.V. thanks the Sharon

Hammes-Schiffer group members, especially Kim Wong and James Watney, for their kindness and help during the realization of this project. S.H.-S. acknowledges support from NSF grant CHE-0096357, AFOSR grant F49620-01-1-0046, and NIH grant GM56207.

Supporting Information Available: Charges used in the models for the S_0 and S_1 states and the modified GROMOS parameters used in the EVB potential. This material is available free of charge via the Internet at <http://pubs.acs.org>.

References and Notes

- (1) Zhong, D.; Douhal, A.; Zewail, A. H. *Proc. Natl. Acad. Sci. U.S.A.* **2000**, *97*, 14056.
- (2) Chattoraj, M.; King, B. A.; Bublit, G. U.; Boxer, S. G. *Proc. Natl. Acad. Sci. U.S.A.* **1996**, *93*, 8362.
- (3) Miskovsky, P. *Int. J. Photoenergy* **2002**, *4*, 45.
- (4) Miskovsky, P. *Curr. Drug Targets* **2002**, *3*, 55.
- (5) Parthenopoulos, D. A.; McMorrow, D. P.; Kasha, M. *J. Phys. Chem.* **1991**, *95*, 2668.
- (6) Möller, S.; Andersen, K. B.; Spanget-Larsen, J.; Waluk, J. *Chem. Phys. Lett.* **1998**, *291*, 51.
- (7) Haddon, R. C.; Stillinger, F. H. In *Molecular Electronic Devices*; Carter, F. L., Ed.; Marcel Dekker: New York, 1987.
- (8) Herek, J. L.; Pedersen, S.; Baares, L.; Zewail, A. H. *J. Chem. Phys.* **1992**, *97*, 9046.
- (9) Frey, W.; Laerner, F.; Elsaesser, T. *J. Phys. Chem.* **1991**, *95*, 10391.
- (10) Lochbrunner, S.; Wurzer, A. J.; Riedle, E. *J. Chem. Phys.* **2000**, *112*, 10699.
- (11) Lochbrunner, S.; Stock, K.; Waele, V. D.; Riedle, E. In *Femtochemistry and Femtobiology*; Douhal, A., Santamaria, J., Eds.; World Scientific: Singapore, 2002; pp 202–212.
- (12) Chudoba, C.; Riedle, E.; Pfeiffer, M.; Elsaesser, T. *Chem. Phys. Lett.* **1996**, *263*, 622.
- (13) Douhal, A.; Lahmani, F.; Zehnacker-Rentien, A.; Amat-Guerri, F. In *Fast Elementary Processes in Chemical and Biological Systems*; Tramer, A., Ed.; American Institute of Physics: Woodbury, NY, 1996; Vol. 346, pp 383–390.
- (14) Guallar, V.; Moreno, M.; Lluch, J. M.; Amat-Guerri, F.; Douhal, A. *J. Phys. Chem.* **1996**, *100*, 19789.
- (15) Douhal, A.; Fiebig, T.; Chacisvilis, M.; Zewail, A. H. *J. Phys. Chem. A* **1998**, *102*, 1657.
- (16) García-Ochoa, I.; Díez-López, M.-A.; Viñas, M. H.; Santos, L.; Martínez-Atáz, E.; Amat-Guerri, F.; Douhal, A. *Chem.—Eur. J.* **1999**, *5*, 897.
- (17) Sytnik, A.; Valle, J. C. D. *J. Phys. Chem.* **1995**, *99*, 13028.
- (18) Ameer-Beg, S.; Ormson, S. M.; Brown, R. G.; Matousek, P.; Towrie, M.; Nibbering, E. T. J.; Fogg, P.; Neuwahl, F. V. R. *J. Phys. Chem. A* **2001**, *105*, 3709.
- (19) Casadesus, R.; Moreno, M.; Lluch, J. M. *Chem. Phys. Lett.* **2002**, *356*, 423.
- (20) Guallar, V.; Batista, V. S.; Miller, W. H. *J. Chem. Phys.* **2000**, *113*, 9510.
- (21) Nagashima, U.; Nagaoka, S.; Katsumata, S. *J. Phys. Chem.* **1991**, *95*, 3532.
- (22) Nagaoka, S.; Nagashima, U. *J. Phys. Chem.* **1991**, *95*, 4006.
- (23) Sobolewski, A. L.; Domcke, W. *Chem. Phys. Lett.* **1993**, *211*, 82.
- (24) Sobolewski, A. L.; Domcke, W. *Chem. Phys. Lett.* **1999**, *300*, 533.
- (25) Duan, X.; Scheiner, S. *Chem. Phys. Lett.* **1993**, *204*, 36.
- (26) Scheiner, S. *J. Phys. Chem. A* **2000**, *104*, 5898.
- (27) Granucci, G.; Hynes, J. T.; Millié, P.; Tran-Thi, T.-H. *J. Am. Chem. Soc.* **2000**, *122*, 12243.
- (28) Petković, M.; Kühn, O. *J. Phys. Chem. A* **2003**, *107*, 8458.
- (29) Li, D. H.; Voth, G. A. *J. Phys. Chem.* **1991**, *95*, 10425.
- (30) Hwang, J. K.; Warshel, A. *J. Phys. Chem.* **1993**, *97*, 10053.
- (31) Borgis, D.; Hynes, J. T. *J. Chem. Phys.* **1991**, *94*, 3619.
- (32) Hammes-Schiffer, S.; Tully, J. C. *J. Chem. Phys.* **1994**, *101*, 4657.
- (33) Ando, K.; Hynes, J. T. *J. Mol. Liq.* **1995**, *64*, 25.
- (34) Mavri, J.; Berendsen, H. J. C. *J. Phys. Chem.* **1995**, *99*, 12711.
- (35) Warshel, A. *J. Phys. Chem.* **1982**, *86*, 2218.
- (36) Villà, J.; Warshel, A. *J. Phys. Chem. B* **2001**, *105*, 7887.
- (37) Warshel, A. *Computer Modeling of Chemical Reactions in Enzymes and Solutions*; Wiley: New York, 1991.
- (38) Vuilleumier, R.; Borgis, D. *Chem. Phys. Lett.* **1998**, *284*, 71.
- (39) Schmitt, U. W.; Voth, G. A. *J. Chem. Phys.* **1999**, *111*, 9361.
- (40) Čuma, M.; Schmitt, U. W.; Voth, G. A. *J. Phys. Chem. A* **2001**, *105*, 2814.
- (41) Billeter, S. R.; Webb, S. P.; Iordanov, T.; Agarwal, P. K.; Hammes-Schiffer, S. *J. Chem. Phys.* **2001**, *114*, 6925.
- (42) Petitpas, I.; Bhattacharya, A. A.; Twine, S.; East, M.; Curry, S. *J. Biol. Chem.* **2001**, *276*, 22804.
- (43) van Gunsteren, W. F.; Billeter, S. R.; Eising, A. A.; Hünenberger, P. H.; Krüger, P.; Mark, A. E.; Scott, W. R. P.; Tironi, I. G. *Biomolecular Simulation: GROMOS96 Manual and User Guide*; BIOMOS b.v., Zürich and Groningen, The Netherlands, 1996.
- (44) Scott, W. R. P.; Hunenberger, P. H.; Tironi, I. G.; Mark, A. E.; Billeter, S. R.; Fennen, J.; Torda, A. E.; Huber, T.; Kruger, P.; van Gunsteren, W. F. *J. Phys. Chem. A* **1999**, *103*, 3596.
- (45) Frisch, M. J.; Trucks, G. W.; Schlegel, H. B.; Scuseria, G. E.; Robb, M. A.; Cheeseman, J. R.; Zakrzewski, V. G.; Montgomery, J. A., Jr.; Stratmann, R. E.; Burant, J. C.; Dapprich, S.; Millam, J. M.; Daniels, A. D.; Kudin, K. N.; Strain, M. C.; Farkas, O.; Tomasi, J.; Barone, V.; Cossi, M.; Cammi, R.; Mennucci, B.; Pomelli, C.; Adamo, C.; Clifford, S.; Ochterski, J.; Petersson, G. A.; Ayala, P. Y.; Cui, Q.; Morokuma, K.; Malick, D. K.; Rabuck, A. D.; Raghavachari, K.; Foresman, J. B.; Cioslowski, J.; Ortiz, J. V.; Stefanov, B. B.; Liu, G.; Liashenko, A.; Piskorz, P.; Komaromi, I.; Gomperts, R.; Martin, R. L.; Fox, D. J.; Keith, T.; Al-Laham, M. A.; Peng, C. Y.; Nanayakkara, A.; Gonzalez, C.; Challacombe, M.; Gill, P. M. W.; Johnson, B. G.; Chen, W.; Wong, M. W.; Andres, J. L.; Head-Gordon, M.; Replogle, E. S.; Pople, J. A. *Gaussian 98*; Gaussian, Inc.: Pittsburgh, PA, 1998.
- (46) Casida, M. E. *Recent Adv. Comput. Chem.* **1995**, *1*, 155.
- (47) Becke, A. D. *J. Chem. Phys.* **1993**, *98*, 5648.
- (48) Foresman, J. B.; Head-Gordon, M.; Pople, J. A.; Frisch, M. J. *J. Phys. Chem.* **1992**, *96*, 135.
- (49) Reed, A. E.; Weinstock, R. B.; Weinhold, F. *J. Chem. Phys.* **1985**, *83*, 735.
- (50) Smith, P. E.; van Gunsteren, W. F. *J. Chem. Phys.* **1994**, *100*, 3169.
- (51) Liu, H.; Mueller-Plathe, F.; van Gunsteren, W. F. *J. Am. Chem. Soc.* **1995**, *117*, 4363.
- (52) Ryckaert, J. P.; Ciccotti, G.; Berendsen, H. J. C. *J. Comput. Phys.* **1997**, *23*, 327.
- (53) Berendsen, H. J. C.; Postma, J. P. M.; van Gunsteren, W. F.; DiNola, A.; Haak, J. R. *J. Chem. Phys.* **1984**, *81*, 3684.
- (54) Fedorowicz, A.; Koll, A.; Mavri, J. *Theor. Chem. Acc.* **2003**, *109*, 220.